Journal of Systems Engineering and Electronics
Vol. 33, No. 4, August 2022, pp.938 – 950

Time-varying baseline error correction method for ground-based micro-deformation monitoring radar

LEI Tianjie[1,2], WANG Jiabao[1,2,3], HUANG Pingping[4,5,*], TAN Weixian[4,5], QI Yaolong[4,5], XU Wei[4,5], and ZHAO Chun[1]

1. China Institute of Water Resources and Hydropower Research, Beijing 100038, China; 2. Institute of Environment and Sustainable Development in Agriculture, Chinese Academy of Agricultural Sciences, Beijing 100083, China; 3. College of Geoscience and Surveying Engineering, China University of Mining and Technology, Beijing 100098, China; 4. College of Information Engineering, Inner Mongolia University of Technology, Hohhot 010051, China; 5. Inner Mongolia Key Laboratory of Radar Technology and Application, Hohhot 010051, China

Abstract: In recent years, ground-based micro-deformation monitoring radar has attracted much attention due to its excellent monitoring capability. By controlling the repeated campaigns of the radar antenna on a fixed track, ground-based micro-deformation monitoring radar can accomplish repeat-pass interferometry without a space baseline and thus obtain high-precision deformation data of a large scene at one time. However, it is difficult to guarantee absolute stable installation position in every campaign. If the installation position is unstable, the stability of the radar track will be affected randomly, resulting in time-varying baseline error. In this study, a correction method for this error is developed by analyzing the error distribution law while the spatial baseline is unknown. In practice, the error data are first identified by frequency components, then the data of each one-dimensional array (in azimuth direction or range direction) are grouped based on numerical distribution period, and finally the error is corrected by the nonlinear model established with each group. This method is verified with measured data from a slope in southern China, and the results show that the method can effectively correct the time-varying baseline error caused by rail instability and effectively improve the monitoring data accuracy of ground-based micro-deformation radar in short term and long term.

Keywords: ground-based micro-deformation monitoring radar, deformation monitoring, time-varying baseline, error compensation.

DOI: 10.23919/JSEE.2022.000091

1. Introduction

Due to influences from external factors (celestial gravity and surface loads) and internal factors (dynamical perturbations of the fluid outer core), the surface deformation of Earth is incessant. At the same time, affected by the growing intensity and frequency of human activities and frequent extreme weather events, the deformation is increasing significantly [1−6]. In this case, landslides, debris flow, ground collapse, and other geological disasters are common all over the world, and has become an important safety hazard in our life and production [7−10]. Therefore, monitoring surface deformation accurately in real time is essential. At present, researchers have developed a variety of instruments for monitoring ground disasters and predicting the evolution of surface deformation [11−14]. Among them, as an active remote sensing monitoring approach, ground-based micro-deformation monitoring radar has attracted much attention due to its long monitoring distance, wide monitoring range, and all-day, all-weather monitoring capability [15−18]. Over the past decades, ground-based micro-deformation monitoring radar has been successfully applied to the cases of slopes, volcanoes, large electric pole towers, and surface collapse [19−23].

In general, some stress changes occur inside the structure of a slope, dam, or other terrain before macroscopic instabilities occur, which are gradually reflected on the surface in the form of surface deformation [24−27]. This process has no time limit and is highly susceptible to extreme weather (strong winds or rain), but it could be predicted if the deformation information were to be captured [21,28−30]. For the ground-based micro-deformation monitoring radar, there are mainly two working modes used for different application scenarios, i.e., the continuous mode and the discontinuous mode. The con-

Manuscript received March 29, 2021.
*Corresponding author.
This work was supported by the National Key R&D Program of China (2018YFC1508502), the National Natural Science Foundation of China (41601569; 61661043; 61631011), and the Science and Technology Innovation Guidance Project of Inner Mongolia Autonomous Region (2019GG139; KCBJ2017; KCBJ 2018014; 2019ZD022).

tinuous mode is suitable for a relatively fixed and risky scene requiring constant monitoring because an instability incident could occur at any time. In contrast, the discontinuous mode allows longer time intervals between rounds of monitoring, which can be applied in a scene where the risk is lower and the target is relatively dispersed. The advantage of the discontinuous mode is that it enables technicians to monitor multiple targets with fewer instruments. It is worth noting that the ground-based micro-deformation monitoring radar requires high baseline accuracy in both modes, creating a thorny problem [31−33]. When the instrument is working in the discontinuous mode, it is difficult to ensure the positions of the instrument coincide exactly in two observations, but any inconsistencies will result in a large baseline error. Although most errors can be removed during data processing by means of image registration and coordinate correction, some will remain. However, even if the instrument is working in the continuous mode, the mechanical disturbance of the platform and the slow creep of the placement point will also lead to a baseline error, and the accumulation of such error cannot be negligible in a long-term observation [34−38].

In summary, it is necessary to carry out time-varying baseline error correction, and data with such error have relatively obvious characteristics. Hence, this paper proposes a method to correct the baseline error of monitoring results when the baseline offset is unknown. The method first identifies the data with baseline error by the numerical distribution information within deformation data. The deformation error data are then decomposed into multiple one-dimensional arrays in the azimuth direction (or in the range direction) based on the error distribution. After that, every one-dimensional array is further decomposed into multiple smaller one-dimensional arrays according to the numerical distribution information of the numerical distribution in it. Finally, the error is corrected with the established models.

This paper is organized as follows: Section 2 describes the study area. Section 3 introduces the core theories and methods, including the calibration process and how to achieve error identification and error correction. Section 4 presents the results. Taking the continuous model as an example, this paper verifies the correction effect of the proposed method under the conditions of short-term monitoring and long-term monitoring with the measured data of a slope in southern China. Section 5 and Section 6 present discussions and conclusions respectively.

2. Theory and study area

2.1 Interference theory

Interferometric measurement is widely used in ground-based micro-deformation monitoring radar. With this technique, the interferometric phase between pixels of the same name is obtained by conjugate multiplication of two radar complex images. Interference phases consist of several components, that is,

$$\phi = \varphi_f + \varphi_t + \varphi_d + \varphi_a + \varphi_{\text{obj}} + \varphi_n \tag{1}$$

where φ_f is the reference plane phase, φ_t is the topographic phase, φ_d is the deformation phase, φ_a is the atmospheric phase, φ_{obj} is the additional phase due to changes in scattering characteristics, and φ_n is the noise. Generally, orbital data, digital elevation model (DEM) data and atmospheric data can be introduced to filter out φ_f, φ_t, and φ_a. If the parameter characteristics of the target before and after deformation remain unchanged, then φ_{obj} can also be ignored. In this case, the composition of the interference phase includes

$$\phi = \varphi_d + \varphi_n. \tag{2}$$

Noise is difficult to filter out, while its value is usually acceptable. Then the interference phase is obtained and the deformation value of the target is calculated based on it [39−42], that is,

$$\Delta R = -\frac{\lambda}{4\pi}(\varphi_d + \varphi_n) \tag{3}$$

where ΔR is the deformation value, and λ is the signal wavelength.

In practice, as Fig. 1 shows, if the distance changes (suppose the center of the instrument moves from O to O'), the baseline error will add a geometric phase to the interferometric phase, which can be regarded as φ_f in (1), that is,

$$\phi_f = -\frac{4\pi(O'P' - OP)}{\lambda} = \frac{4\pi d \sin\beta}{\lambda \sin(\beta - \alpha)} \tag{4}$$

where β is the slope inclination, α is the angle between the radar line of sight (LOS) and the horizontal line, and it can be seen that φ_f is influenced by the baseline offset, the distance and visual angle between the radar and the target, and the shape of the target surface.

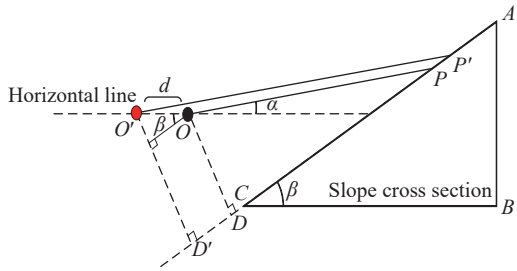

Fig. 1 Schematic diagram of the impact of instrument instability on monitoring

It is worth mentioning that, due to the periodicity of trigonometric functions, the phase difference we end up with is the phase principal value, which is also known as the wrapped phase and is limited to the range $[-\pi,+\pi]$. If the baseline error is so large that the additional geometric phase exceeds the range $[-\pi,+\pi]$, the phase difference will vary periodically within it [43−46]. As for traditional approaches, this type of error is often considered as simple low-frequency signal filtering, as its numerical distribution shows the distinct characteristic of a large-amplitude and low-frequency signal [31,38]. However, the numerical jump of the phase at $\pm\pi$ prevents simple filtering from being able to completely eliminate the error. And it is also difficult to eliminate the baseline error from the source while the offset and direction of the instrument movement are random and unknown.

2.2 Study area

The study area of this paper is a slope located in southern China, it is composed of a large mass of soil, detritus and a large expensed rock wall which is generated by a massive landslide.

As presented in Fig.2(a), the stability of the slope needs to be monitored in real time as the engineers reinforce the exposed rock wall and treat the slope and its surrounding facilities. The engineers also place guardrails on the rock walls to protect workers and equipment from rock falling.

(a) Partition diagram of monitoring target

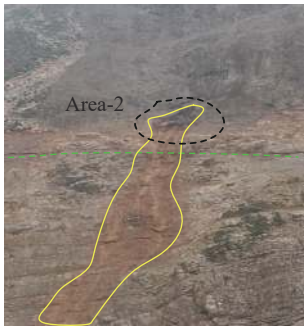

(b) Schematic diagram of Area-2

——: Exposed rock wall; ——: Reinforced area;
——: Terrene slope; ——: Guardrail.

Fig. 2 Schematic diagram of monitoring target

The ground-based micro-deformation monitoring radar was developed by Inner Mongolia Mypattern Technology Co., Ltd., which was placed at a position of about 200 m to the observed area on the south side of the slope. It mainly adopts the synthetic aperture technique and the differential interferometry technique, and it can obtain the deformation information of the whole slope at one time. It works at a frequency of Ku band. Some parameters of the instrument are shown in Table 1.

Table 1 Instrument parameters

Parameter	Value
Bandwidth/MHz	500
Field of view/(°)	>60 (azimuth)×30 (elevation)
Repetition time/min	8
Resolution	0.3 m× 5.4 mrad

During the monitoring process, the instrument was unstable due to ground construction and earthquake, and thus time-varying baseline error occurred in the monitoring data. The monitoring area experienced several intense precipitations in July 2019, resulting in instability in two areas on the slope, denoted as Area-1 and Area-2 in Fig. 2. These two cases provided multiple types of data for this study, and the timing continuity of the data was good. Finally, the data from July 15, 2019 to July 31, 2019, were selected as measured cases for demonstration.

3. Materials and methods

3.1 Data-processing flow

The processing flow of the method proposed in this paper is shown in Fig. 3. The process can be divided into two parts. First, it should be determined whether the data contain baseline errors, and then any errors should be corrected. In practical monitoring, deviations of the instrument's orientation may lead to different distribution modes of the error (along the range direction or along the azimuth direction). In addition, the shape of the monitoring target surface may make it difficult for the radar signal to reach some certain areas, thus resulting in fade areas. Therefore, it is necessary to select multiple one-dimensional arrays at equal intervals along two directions in the deformation data to ensure that the information is not omitted due to missing data. To be specific, several one-dimensional arrays are first selected in the range direction at equal intervals after obtaining deformation data, and the fast Fourier transform (FFT) is applied. Then it is judged whether there is a low-frequency component with a large amplitude in the entire frequency

component. If so, it means that there is baseline error in the data, which should be corrected. If not, we should select several one-dimensional arrays at equal intervals in the azimuth direction and conduct the same operations as in the range direction. Once there is no obvious low-frequency component with large amplitude in the range direction and azimuth direction, the data are free of baseline error.

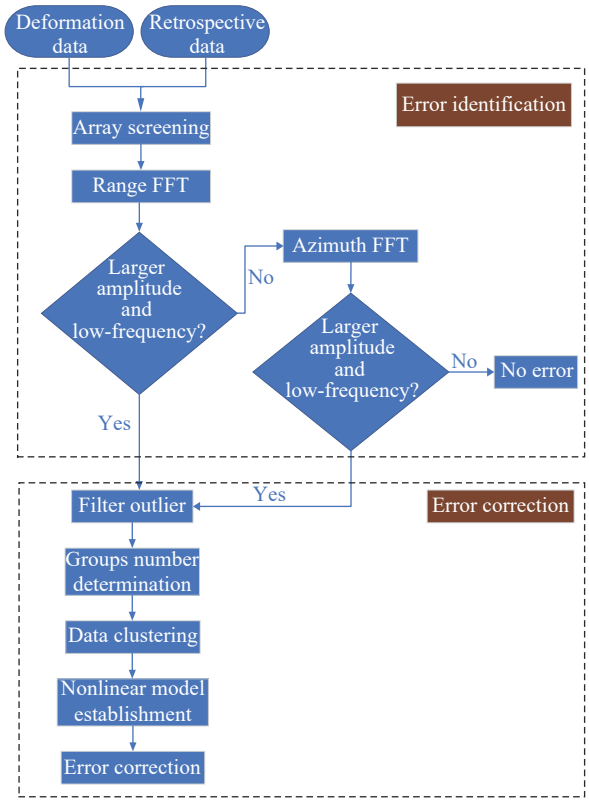

Fig. 3 Flow chart of error identification and error correction

The purpose of clustering and grouping the data is to avoid the difficulties caused by the numerical jump at $\pm\pi$. Furthermore, to improve the accuracy of data clustering, outliers in the data should be filtered out. In the method proposed in this paper, we hope that the data of each period can be divided into a separate group, and the number of groups depends on the number of phase wrap cycles, which can also be estimated by the frequency component of data. After that, the value distribution in each group should be monotonically increasing (or decreasing). Nevertheless, this trend is not necessarily linear due to the influence of the target surface shape, thus a nonlinear model is established according to the trend, and the error is finally corrected by the model.

In addition, Fig.4 shows two kinds of data that can be used in the above processing: deformation data and review data. Deformation data represents the real-time state of the observed area, which reflects the difference between the echo data of two adjacent campaigns. Nevertheless, if the instrument is shifted at a slow rate, the error may be not obvious enough to present in the real-time data. At this time, two echo data with a longer time interval which called review data in this paper can be adopted in the difference processing so as to observe the cumulative result of the error. Even more important is that the time interval mentioned above must be well limited. If the interval is too long, the accumulated error may become larger and lead to multiple periods wrapped phase, or even lose the true deformation value of the target during this interval [47−50]. The appropriate interval should be chosen with reference to the specific situation in practice.

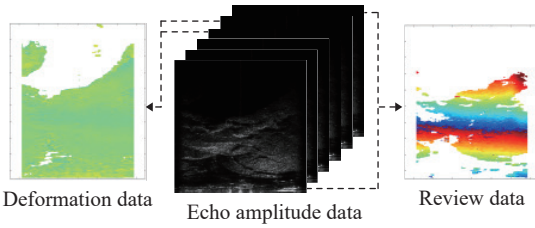

Fig. 4 Deformation data and review data

3.2 Error identification

As mentioned above, the time-varying baseline error cannot be simply filtered as a low-frequency signal, but it can still be identified based on this feature. Suppose the selected one-dimensional array is V, and then the frequency component for V needs to be analyzed, that is,

$$F((A_1,f_1),(A_2,f_2),\cdots,(A_{n-1},f_{n-1}),(A_n,f_n)) = \mathrm{fft}(V) \quad (5)$$

where A_n and f_n are the amplitude and frequency for each component respectively, n ($n\in\mathbf{N}^+$) is affected by the sampling frequency f_s and the number of sampling points N, and fft(·) is the FFT function. To observe the frequency components in V further completely, more sampling points and a higher sampling frequency can be adopted. If the obtained frequency component contains a large amplitude signal with low frequency, the data contain errors. Nevertheless, it should be noted that neither the large amplitude nor the low frequency adopted here is an absolute standard, meaning their values are different in different monitoring scenarios. Therefore, it is more appropriate to consider the statistical result of real-time data in practice and the prior information when setting the amplitude threshold T_A and frequency threshold T_f.

3.3 Error correction

In spaceborne and airborne interferometry, a common method is to establish an appropriate mathematical model

based on the error distribution and to remove the error with the fitting data obtained by the model [51]. It is quite difficult, though, to build a highly accurate mathematical model due to the influence of multiple sources of error and observation blind area on data. However, the area studied in this manuscript is small and has not undergone drastic topographic changes. This makes the error caused by baseline instability very similar to the flat bottom effect of interference processing in spaceborne and airborne conditions. It is also could be noticed that, in this case, the error distribution along the distance direction was regular, and the data in different directions had a good correlation. This greatly simplifies model building, and it allows for error correction row by row or column by column.

Another problem is that, due to terrain changes and periodic phase changes, the error value will repeatedly jump at a phase equal to $\pm\pi$. If each period can be separated from the wrapped phase, then each separated dataset will present a simple monotone nonlinear change, and its mathematical modeling will also be simple. Therefore, the key step of the proposed method for error correction in this paper is to firstly separate out each period of the one-dimensional array V and then establish mathematical models for correction. The process can be divided into the following steps.

3.3.1 Outliers filtration

The accuracy of separating will directly affect the correction result, and it will help to improve the accuracy if the numerical distribution trend of V is clear, or the number of the wrapped period is known. Therefore, outliers in V need to be filtered out.

Since the numerical difference between a outlier and its adjacent element is usually larger than that of the normal adjacent elements, and the difference value of normal adjacent elements that in a same period is smaller, the standard deviation of the difference value for adjacent elements in V can be used as the threshold for identifying outliers. That is,

$$T_{\text{out}-1}=\sum_{j=2}^{m}\left(\left(\frac{\sum_{i=2}^{m}(V_i-V_{i-1})}{m}\right)-(V_j-V_{j-1})\right)^2\Big/m \tag{6}$$

where $T_{\text{out-1}}$ is the recognition threshold, and m is the elements number of V. The point can be considered as an outlier as long as its numerical difference with any adjacent element is greater than this threshold (the value of the element in the fade area is considered to be 0), and the value of the outliers will be set to zero.

3.3.2 Numerical clustering

Since the period of the wrapped phase should be very close to the period of the low-frequency component with the maximum amplitude, the frequency component analysis of the filtered V, named V_{filter} in the following, will be helpful to determine the number of the wrapped period, specificly:

$$N_p=\lfloor m_a/f_{\max}(A)\rfloor \tag{7}$$

where N_p is the number of the wrapped period, and m_a is the sequence length of non-zero elements within V, which is equal to the coordinate numerical difference between the last non-zero element and the first non-zero element in V, and $f_{\max}(A)$ is the frequency of the component with the largest amplitude. The periods number should be equal to the groups number. Similar to the method of removing outliers, this paper mainly depends on the numerical difference between adjacent non-zero elements in the clustering process, but the threshold value at this time should be obtained by V_{filter}, that is,

$$T_{\text{out}-2}=\sum_{j=2}^{m}\left(\frac{\sum_{i=2}^{m}(V_{\text{filter},i}-V_{\text{fiter},i-1})}{m}-(V_{\text{filter},j}-V_{\text{filter},j-1})\right)^2\Big/m \tag{8}$$

where $T_{\text{out-2}}$ is the threshold for clustering, and this process should be carried out from the first non-zero element of V_{filter}. They will be considered to belong to the same group if the absolute difference value of two adjacent non-zero elements is less than $T_{\text{out-2}}$; otherwise, they will be respectively assigned to the two adjacent groups. Furthermore, it should be noted that the data in a same period may be discontinuous, but the trend should be consistent. Therefore, the threshold actually used in this process is $c\times T_{\text{out-2}}$, where c is the coordinate interval between two adjacent non-zero elements. Obviously, it is established on the premise that the value in a single period changes linearly, but in fact the time-varying baseline error usually shows a nonlinear change. It means if there is a long data discontinuous in V_{filter}, the linear growth rate of $T_{\text{out-2}}$ threshold may be too high, and thus leading to the wrong clustering. Based on the statistical results of actual data, this paper sets the upper limit of the growth of this threshold, which is not more than half of the maximum value in V_{filter}, that is,

$$\begin{cases} T_{\text{out}-v}=cT_{\text{out}-2} \\ T_{\text{out}-v}\leqslant\dfrac{1}{2}\max\ V_{\text{filter}} \end{cases}. \tag{9}$$

Clustering is easy to implement when only one or two periods exist in the data, since the elements only need to be organized into one or two groups. However, if the number of periods is greater than two, another decision condition needs to be added in the clustering to determine whether the element assigned to a group will obey the monotonicity formed by the existing element in the group. For example, if the numerical distribution in V_{filter} is three periods, then it should be split into three groups. When the difference between an element and the last element of the first group is greater than $T_{\text{out-v}}$, the element should be assigned to the second group. When the difference between an element and the last element of the second group is greater than $T_{\text{out-v}}$, then it should be determined whether the value of the element obeys the monotonicity formed by the existing element in the first group; if not, the element should be assigned to the third group. Generally, the elements in two nonadjacent periods will not cross each other. Thus, the clustering of the first group has been completed when the third group has an element allocated.

3.3.3 Least squares (LS) numerical fitting

Each group obtained by clustering can be represented by a nonlinear mathematical model, that is,

$$S(x) = a_0\varphi_0(x) + a_1\varphi_1(x) + a_2\varphi_2(x) \tag{10}$$

where a_0, a_1, a_2 are the coefficients of the model, and $\varphi_0(x)$, $\varphi_1(x)$, $\varphi_2(x)$ are linearly independent function clusters. In this paper, it can be considered as $\varphi_0(x) = 1$, $\varphi_0(x) = x$, and $\varphi_0(x) = x^2$ when a second-order nonlinear mathematical model is adopted [52]. The LS method is adopted to solve the coefficients of the model, which assumes the existence of a cluster value $\boldsymbol{\delta}$ as follows:

$$\|\boldsymbol{\delta}\|_2^2 = \min \sum_{i=0}^{2} (S(x_i) - f(x_i))^2 \tag{11}$$

where $f(x_i)$ is the value of the original function. To make model $S(x)$ to approximate the original value as close as possible, $\boldsymbol{\delta}$ should be as small as possible, and it will reach the best case if $S(x_i)$ is equal to $f(x_i)$. Nevertheless, this is impossible for an irregular function, so it turns into a problem of finding a minimum value for a function with several variables, and can be solved by $\boldsymbol{Ga}=\boldsymbol{d}$, that is,

$$\begin{cases} \boldsymbol{a} = [a_0 \quad a_1 \quad a_2]^{\mathrm{T}} \\ \boldsymbol{d} = [d_0 \quad d_1 \quad d_2]^{\mathrm{T}} \\ \boldsymbol{G} = \begin{bmatrix} (\varphi_0,\varphi_0) & (\varphi_0,\varphi_1) & (\varphi_0,\varphi_2) \\ (\varphi_1,\varphi_0) & (\varphi_1,\varphi_1) & (\varphi_1,\varphi_2) \\ (\varphi_2,\varphi_0) & (\varphi_2,\varphi_1) & (\varphi_2,\varphi_2) \end{bmatrix} \end{cases}. \tag{12}$$

The solutions of (φ_j, φ_k) and d_k are as follows:

$$\begin{cases} (\varphi_j,\varphi_k) = \sum_{i=0}^{2} \varphi_j(x_i)\cdot\varphi_k(x_i) \\ (f,\varphi_k) = \sum_{i=0}^{2} f(x_i)\cdot\varphi_k(x_i) = d_k,\ k = 0,1,2 \end{cases}. \tag{13}$$

The complete expression of model $S(x)$ can be obtained when the coefficients a_0, a_1, a_2 are calculated by (12) and (13), and then the error correction can be completed by subtracting model $S(x)$ from the original array V. It should be noted that since V may contain more than one $S(x)$, multiple sections are required for error correction. The outliers that are filtered out in the first step of the error correction should also participate in the process and be corrected by the model with the closest values. Moreover, all the expositions and processes mentioned above will be presented more intuitively in the results section.

4. Results

This section presents the verification results of the proposed method using measured data of a slope in southern China. The instrument used in this project is affected by construction, earthquake, and other factors during the monitoring period, and it successfully detects two landslides, so the instrument provids abundant and reliable measured data for this study. Subsection 4.1 presents the results of error identification and compares the characteristic differences between different types of data. In Subsection 4.2, the effect of error correction is shown from the perspectives of short-term and long-term monitoring.

4.1 Error identification results

This subsection presents the frequency analysis results of three types of data: data with no baseline error and no significant deformation, data with no baseline error but significant deformation, and data with significant baseline error (for brevity, they will hereafter be called Type-1, Type-2, and Type-3). In the frequency analysis process, several one-dimensional arrays are taken from each type of data, and their frequency components are compared. The results are shown in Fig. 5. The deformation maps of the three types of data selected are shown in Fig. 5(a), Fig. 5(d), and Fig. 5(g), while the corresponding selected one-dimensional arrays are marked with red dotted lines in the figures. It can be seen from Fig. 5(b) that small amplitude of numerical fluctuation occurs at 50–100 m from the instrument, which likely reflects the influence of ground construction activities. Meanwhile, as shown in Fig. 5(b) and Fig. 5(c), the data amplitude is small, and so is the amplitude of the low-frequency component. When the selected one-dimensional array passes through a deformation area in the monitoring scene, it brings a large

peak to the numerical distribution in an appropriate position, as shown in Fig. 5(e), so the amplitude of the low-frequency component in the array also increases. Finally, the numerical distribution shows obvious periodicity (as shown in Fig. 5(h)) when there is a baseline error, and the amplitude of the low-frequency component is significantly greater than that of the other two types of data. In addition, it can be seen from Fig. 5(g) that, due to the uneven distribution of the actual terrain, there is a case of repeated numerical jumps at the position of phase wrap, which makes the two adjacent periods intersect and increases the difficulty of clustering.

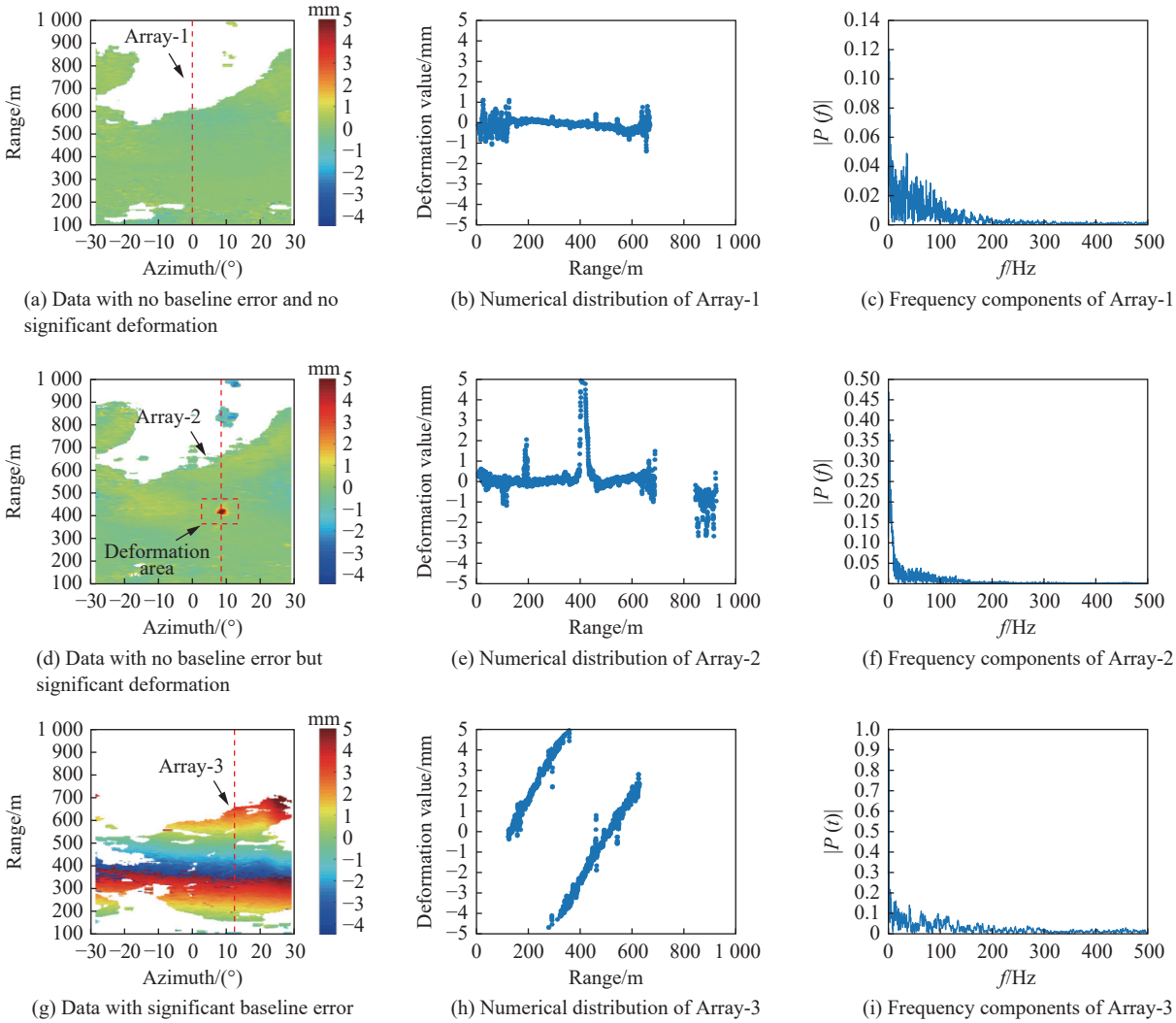

(a) Data with no baseline error and no significant deformation
(b) Numerical distribution of Array-1
(c) Frequency components of Array-1
(d) Data with no baseline error but significant deformation
(e) Numerical distribution of Array-2
(f) Frequency components of Array-2
(g) Data with significant baseline error
(h) Numerical distribution of Array-3
(i) Frequency components of Array-3

Fig. 5 Characteristics of different types of data

The amplitude distribution of the low-frequency components of different types of data can be obtained according to the above analysis. Images of 1 330 scenes are calculated to further verify the rule, and the results are shown in Table 2. This statistic helps to determine the threshold T_A, which is used to identify the error data, as the peak value 0.6 is the boundary line between Type-3 and the other two types. Thus, it should be the appropriate value to determine if the monitoring data for the study area contains baseline error. In practice, engineers do not need to update the threshold in real time. They only need to give a reference threshold applicable to the current region by monitoring the initial data statistics.

Table 2 Amplitude peak distribution of low-frequency components for different types of data %

Peak value	Type-1	Type-2	Type-3
0.0−0.3	88.3	23.2	0.0
0.3−0.6	11.7	76.8	0.0
0.6−1.0	0.0	0.0	47.2
>1.0	0.0	0.0	52.8

4.2 Error identification results

According to the method introduced above, this section selects two one-dimensional arrays from the data, namely, Array-5 and Array-6. We take range direction as an example to present the error correction process. Among them, Array-5 passes through a small deformation area caused by construction, denoted as Area-3, while Array-6 passes through no deformation area. At the same time, it can be clearly seen that the error value in the data transforms two cycles, so the clustering result should be two groups. The details are shown in Fig. 6. The two intersecting cycles are accurately divided into two groups, and the numerical distribution in each group is very clear, so it is easy to establish the mathematical model. In addition, it can be seen from Fig. 6(e) and Fig. 6(f) that the value of Area-3 still maintains an original relative relation with the values of its adjacent pixel points, indicating that the process retains the real deformation information when correcting errors.

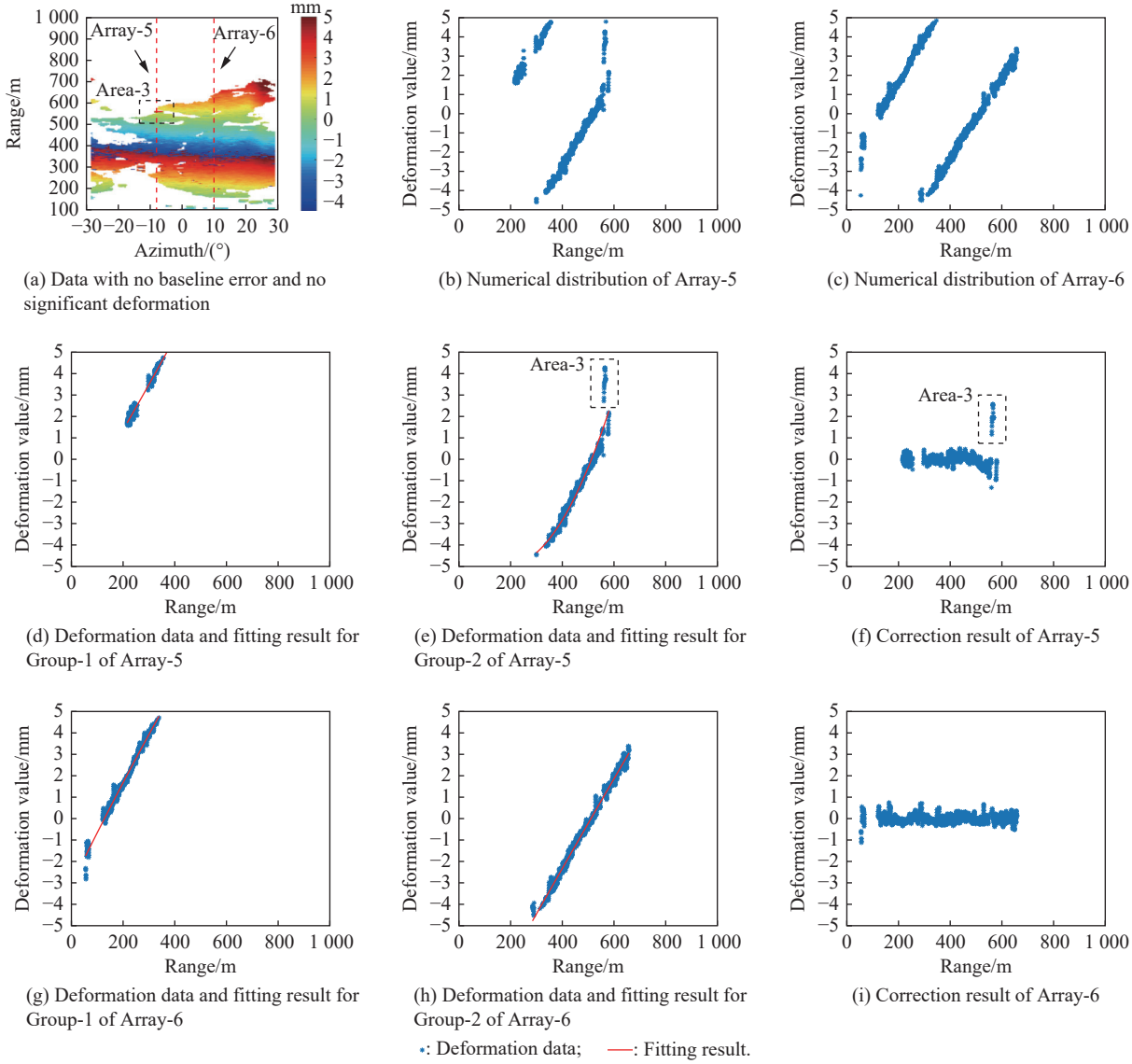

(a) Data with no baseline error and no significant deformation

(b) Numerical distribution of Array-5

(c) Numerical distribution of Array-6

(d) Deformation data and fitting result for Group-1 of Array-5

(e) Deformation data and fitting result for Group-2 of Array-5

(f) Correction result of Array-5

(g) Deformation data and fitting result for Group-1 of Array-6

(h) Deformation data and fitting result for Group-2 of Array-6

(i) Correction result of Array-6

Fig. 6 Example for error correction process

After the above processing for each one-dimensional array in the data to be corrected, a complete error correction can be achieved, with the results shown in Fig. 7(a). It is obvious that the original obvious baseline error is well corrected, while Area-3 retains the relatively complete deformation information. Fig. 7(b) presents the correction results for short-term data, while Fig. 8(a) presents the correction results for long-term deformation

accumulation. It can be seen that there are two deformation areas in the monitoring scene. In fact, the occurrence time of these two areas of deformation is inconsistent, because the method deals with each single interference result in the process of processing, rather than the accumulation of multiple interference results. At the same time, when the data collection period of the equipment is short enough, the numerical change caused by the deformation will not exceed $\lambda/4$, and there will not be a large numerical mutation. Therefore, this method is feasible when there are multiple deformation regions in the scene. The obvious negative deformation occurred in the reinforcement area and the ground construction area, as shown in Fig. 8(a). However, large area deformation did not occur, this indicated that the monitoring data are affected by the instability of the instrument and would seriously mislead the stability judgment. However, there are many discrete deformation points or point sets due to the frequent human activities, construction, and many unstable scattered gravel pieces in the monitoring scene, which cannot be ignored.

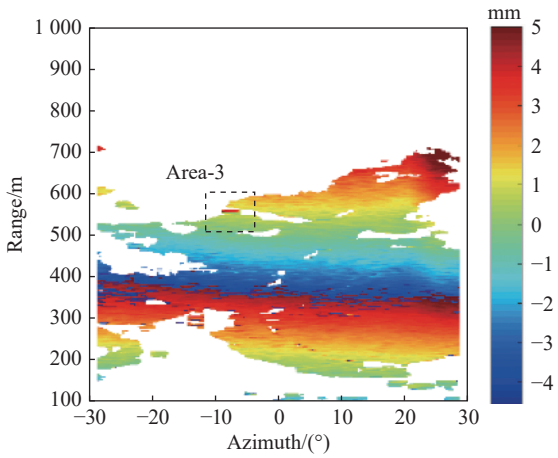

(a) Deformation before correction

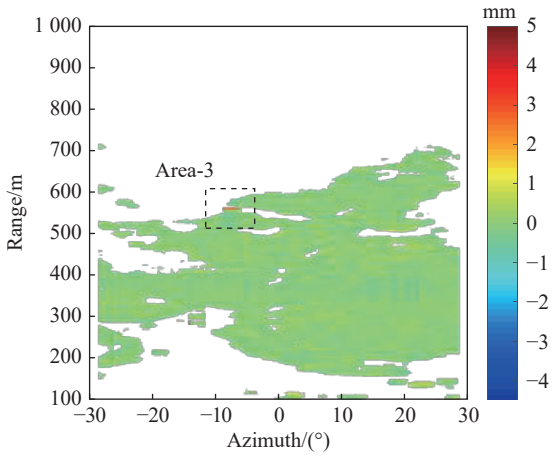

(b) Deformation after correction

Fig. 7 Deformation data comparison before and after correction

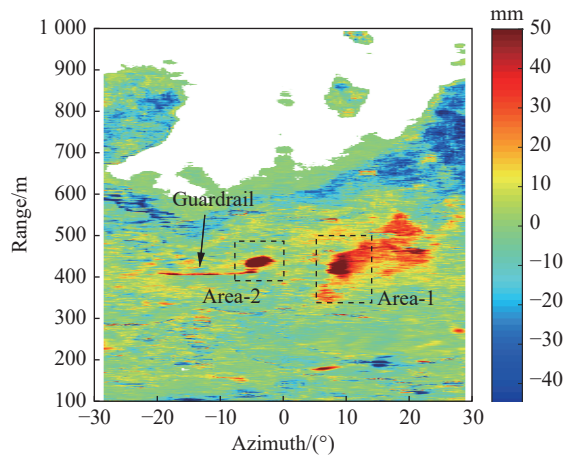

(a) Cumulative deformation before correction

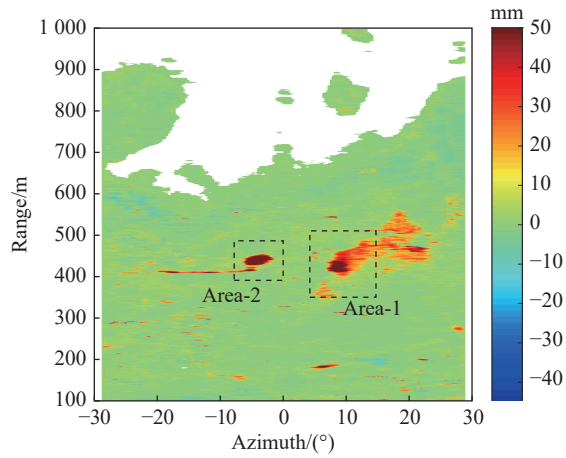

(b) Cumulative deformation after correction

Fig. 8 Cumulative deformation before and after correction within half a month

However, in slope stability monitoring, it is not worth worrying about if the target cumulative value is only caused by a sudden change in the deformation value at a certain time, because it is likely that the monitoring data are interfered with human activity [53]. The areas of interest are Area-1 and Area-2, which are out of the human activity range and exhibit continuous deformation. Finally, it can be found through comparison that the correction method of long-term accumulated data proposed in this paper can get good correction of errors and retain the deformation information of Area-1 and Area-2. In addition, it can be seen from Fig. 8 that there is a linear deformation zone below Area-2, which corresponds to the guardrail in Fig. 2(a). This indicates that stones falling from Area-2 are intercepted by the protective fence. Although the impact force of the falling stones causes the guardrail to deform, the guardrail successfully protects the staff and equipment.

5. Discussions

According to the working principle and measured data of the ground-based micro-variation monitoring radar, this study illustrates that time-varying baseline error has a significant impact on the accuracy and reliability of monitoring data. The measured data used in this study are collected in the continuous mode, and the time-varying baseline error in this mode may be caused by construction, instrument instability caused by earthquake, and mechanical disturbance, which may be without great impact but relatively frequent. The errors generated by different causes differ in amplitude and frequency, so there is a variety of error data superimposed on each other in the long-term data accumulation, making the frequency components in the accumulated data extremely complex, and thus making the error correction difficult. In view of this situation, this study suggests that data review should be carried out before data accumulation, and the selection of time interval during the review process should be carefully considered. In general, longer time intervals may make the time-varying baseline errors in the data more apparent, thus making clustering and modeling easier and correcting results more accurate. However, excessive time intervals may cause time de-coherence, resulting in the loss of some key data, especially when the target is deformed. In contrast, short time intervals can ensure good coherence but may not be enough to highlight the time-varying baseline error. Therefore, this study chooses a relatively flexible strategy in the accumulation of measured data: if the target is relatively stable, a longer time interval can be selected during the data review, and if the target is deformed, a shorter time interval can be adopted. Fig. 8 shows the results when 2 h/8 min (stable stage/deformation stage) is used as the time interval of data review.

To further illustrate the correction results at different time intervals, Fig. 9 shows the cases in which the time intervals are 2 h/30 min and 1 h/8 min. It can be seen from Fig. 9(a) that adopting a longer time interval when the target is deformed will indeed result in the loss of deformation information, and Fig. 9(b) indicates that using a shorter time interval during the stability stage may retain more errors.

The selection of specific values should be determined after the monitoring target is fully monitored and analyzed. The inversion analysis can be used to determine whether the monitoring target is stable or deformed in a certain period.

Finally, special attention should be paid to the stability of the instrument so that the time-varying baseline error can be corrected. If the instrument is operating in the discontinuous mode, the reference points of the two campaigns should coincide as much as possible to minimize the impact of the time-varying baseline error on monitoring. It should be noted that the influence of atmospheric changes on monitoring results is not considered in this study since an atmospheric correction processing module has been added to the test instrument used in this study [54]. The introduction of atmospheric delay will complicate the calibration model, which will be the focus of our future work.

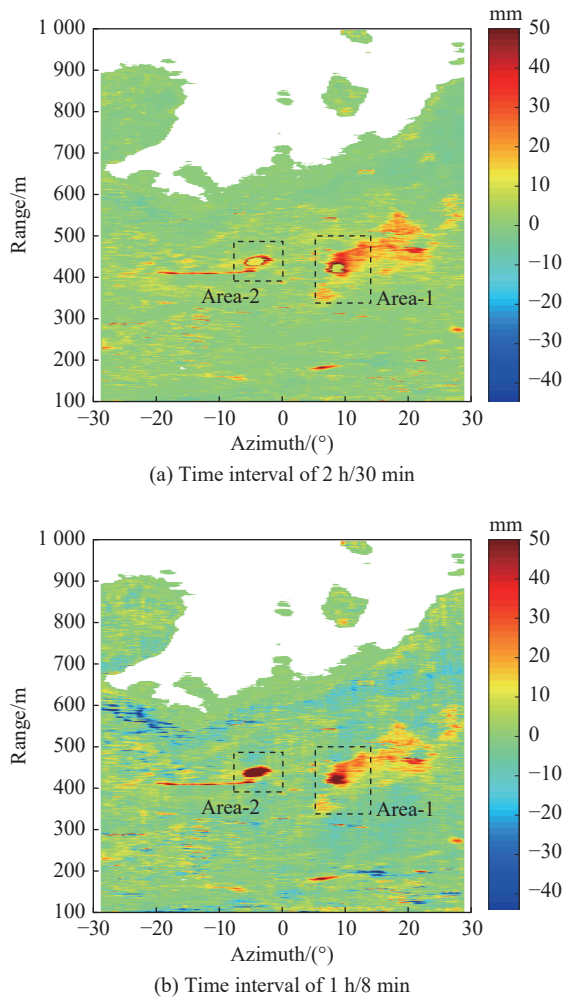

(a) Time interval of 2 h/30 min

(b) Time interval of 1 h/8 min

Fig. 9 Correction cumulative deformation data comparison in different time interval

6. Conclusions

The stability of the ground-based micro-deformation monitoring radar is important to obtain accurate deformation information, as additional time-varying baseline error may lead to misjudgment by the monitoring system or observers if the instrument is unstable. Although engineers attach great importance to the stability of the ground-based micro-deformation monitoring radar in practi-

cal monitoring, it is difficult to eliminate instability during the monitoring period, so it is necessary to correct the time-varying baseline error. The method proposed in this paper aims to correct time-varying baseline error under the condition that the space baseline is unknown. It can identify the data affected by time-varying baseline error according to the frequency and the numerical distribution information, disintegrate the data into several parts to simplify the mathematical model, and achieve error correction. The data after correction will be more accurate and reliable, which will help observers and engineers more accurately judge slope stability, especially in the process of long-term deformation accumulation. According to successful validation with the measured data of a slope in southern China, the proposed method can accurately identify data containing errors, and the data quality after correction can reach the level of normal data while relatively complete deformation information is retained. Overall, the method in this paper has good feasibility and effectiveness both in short-term and long-term monitoring.

References

[1] BURGMANN R, ROSEN P A, FIELDING E J. Synthetic aperture radar interferometry to measure Earth's surface topography and its deformation. Annual Review of Earth and Planetary Sciences, 2000, 28(1): 169–209.

[2] XU J Q, SUN H P. Earth's deformation due to the dynamical perturbations of the fluid outer core. Acta Seismologica Sinica, 2002, 15(4): 414–424.

[3] FROUDE M J, PETLEY D N. Global fatal landslide occurrence from 2004 to 2016. Natural Hazards and Earth System Sciences, 2018, 18(8): 2161–2181.

[4] ZHANG M, NIE L, XU Y, et al. A thrust load-caused landslide triggered by excavation of the slope toe: a case study of the Chaancun landslide in Dalian city, China. Arabian Journal of Geosciences, 2015, 8(9): 6555–6565.

[5] SAITO H, KORUP O, UCHIDA T, et al. Rainfall conditions, typhoon frequency, and contemporary landslide erosion in Japan. Geology, 2014, 42(11): 999–1002.

[6] LIU J K, SHIH P T. Topographic correction of wind-driven rainfall for landslide analysis in central Taiwan with validation from aerial and satellite optical images. Remote Sensing, 2013, 5(6): 2571–2589.

[7] VAN DER GEEST K. Landslide loss and damage in Sindhupalchok District, Nepal: comparing income groups with implications for compensation and relief. International Journal of Disaster Risk Science, 2018, 9(2): 157–166.

[8] PAUDEL P P, OMURA H, KUBOTA T, et al. Landslide damage and disaster management system in Nepal. Disaster Prevention and Management, 2003, 12(5): 413–419.

[9] BAJEK R, MATSUDA Y, OKADA N. Japan's Jishu-bosai-soshiki community activities: analysis of its role in participatory community disaster risk management. Natural Hazards, 2008, 44(2): 281–292.

[10] HUANG M, QI S Z, SHANG G D. Karst landslides hazard during 1940 –2002 in the mountainous region of Guizhou Province, Southwest China. Natural Hazards, 2012, 60(2): 781–784.

[11] EDVIN A, DJAMIL Y S. Application of multivariate Anfis for daily rainfall prediction: influences of training data size. Makara Journal of Science, 2008, 12(1): 7–14.

[12] ATZENI C, BARLA M, PIERACCINI M. Early warning monitoring of natural and engineered slopes with ground-based synthetic-aperture radar. Rock Mechanics and Rock Engineering, 2015, 48(1): 235–246.

[13] CARLA T, INTRIERI E, DI T F, et al. Guidelines on the use of inverse velocity method as a tool for setting alarm thresholds and forecasting landslides and structure collapses. Landslides, 2017, 14(2): 517–534. (in Chinese)

[14] XU Q, TANG M G, HUANG R Q. Monitoring, early warning and emergency disposal of large landslides. Beijing: Science Press, 2015. (in Chinese)

[15] BO H, CHEN J Y, ZHANG X F. Monitoring the land subsidence area in a coastal urban area with InSAR and GNSS. Sensors, 2019, 19(14): 3181.

[16] WANG Y P, HONG W, ZHANG Y, et al. Ground-based differential interferometry SAR: a review. IEEE Geoscience and Remote Sensing Magazine, 2020, 8(1): 43–70.

[17] PIERACCINI M, MICCINESI L, ROJHANI N. A GBSAR operating in monostatic and bistatic modalities for retrieving the displacement vector. IEEE Geoscience and Remote Sensing Letters, 2017, 14(9): 1494–1498.

[18] GE D Q, DAI K R, GUO Z C, et al. Early identification of serious geological hazards with integrated remote sensing technologies: thoughts and recommendations. Geomatics and Information Science of Wuhan University, 2019, 44(7): 949–956. (in Chinese)

[19] HU F M, WU J C. Detecting spatio-temporal urban surface changes using identified temporary coherent scatterers. Journal of Systems Engineering and Electronics, 2021, 32(6): 1304–1317.

[20] FLORENTINO A, CHARAPAQUI S, JARA C, et al. Implementation of a ground-based synthetic aperture radar (GB-SAR) for landslide monitoring: system description and preliminary results. Proc. of the IEEE XXIII International Congress on Electronics, Electrical Engineering and Computing, 2016: 1–6.

[21] GRAHAM J D, ERIK E. Development of an early-warning time-of-failure analysis methodology for open-pit mine slopes utilizing ground-based slope stability radar monitoring data. Canadian Geotechnical Journal, 2015, 52(4): 515–529.

[22] ASLAN G, FOUMELIS M, RAUCOULES D. Landslide mapping and monitoring using persistent scatterer interferometry (PSI) technique in the French Alps. Remote Sensing, 2020, 12(8): 1305.

[23] TRAGLIA F, INTRIERI E, NOLESINI T, et al. The ground-based InSAR monitoring system at Stromboli volcano: linking changes in displacement rate and intensity of persistent volcanic activity. Bulletin of Volcanology, 2014, 76(2): 786.

[24] SOGA K, ALONSO E, YERRO A, et al. Trends in large-deformation analysis of landslide mass movements with particular emphasis on the material point method. Geotechnique, 2016, 66(3): 248–273.

[25] ZENG T, DENG Y K, HU C, et al. Development state and application examples of ground-based differential interferometric radar. Journal of Radars, 2019, 8(1): 154–170.

[26] LI W L, XU Q. Historical retrospection of deformation of large rocky landslides and its enlightenment. Geomatics and Information Science of Wuhan University, 2019, 44(7): 1043–1053. (in Chinese)

[27] SIDLE R C, BOGAARD T A. Dynamic earth system and ecological controls of rainfall-initiated landslides. Earth-sci-

ence Reviews, 2016, 159: 275–291.
[28] DAI K R, LI Z H, XU Q, et al. Entering the era of earth observation-based landslide warning systems: a novel and exciting framework. IEEE Geoscience and Remote Sensing Magazine, 2020, 8(1): 136–153.
[29] GLASTONBURY J, FELL R. Geotechnical characteristics of large slow, very slow, and extremely slow landslides. Canadian Geotechnical Journal, 2008, 45(7): 984–1005.
[30] QIN S Q, WANG Y Y, MA P. Exponential laws of critical displacement evolution for landslides and avalanches. Chinese Journal of Rock Mechanics and Engineering, 2010, 29(5): 873–880. (in Chinese)
[31] CROSETTO M, MONSERRAT O, LUZI G, et al. Discontinuous GBSAR deformation monitoring. ISPRS Journal of Photogrammetry and Remote Sensing, 2014, 93: 136–141.
[32] YIGIT E, DEMIRCI S, OZDEMIR C, et al. Short-range ground-based synthetic aperture radar imaging: performance comparison between frequency-wavenumber migration and back-projection algorithms. Journal of Applied Remote Sensing, 2013, 7(1): 073483.
[33] MONSERRAT O, CROSETTO M, LUZI G. A review of ground-based SAR interferometry for deformation measurement. ISPRS Journal of Photogrammetry and Remote Sensing, 2014, 93: 40–48.
[34] PAN X D, XU Y M, XING C, et al. Study of a GB-SAR rail error correction method based on an incident angle model. IEEE Trans. on Geoscience and Remote Sensing, 2019, 58(1): 510–518.
[35] YANG H L, CAI J W, PENG J H. A correcting method about GB-SAR rail displacement. International Journal of Remote Sensing, 2017, 38(6): 1483–1493.
[36] HU C, ZHU M, ZENG T, et al. High-precision deformation monitoring algorithm for GBSAR system: rail determination phase error compensation. Science China Information Sciences, 2016, 59(8): 082307.
[37] CROSETTO M, MONSERRAT O, LUZI G, et al. A noninterferometric procedure for deformation measurement using GB-SAR imagery. IEEE Geoscience and Remote Sensing Letters, 2013, 11(1): 34–38.
[38] WANG Z, LI Z H, MILLS J. Modelling of instrument repositioning errors in discontinuous multi-campaign ground-based SAR (MC-GBSAR) deformation monitoring. ISPRS Journal of Photogrammetry and Remote Sensing, 2019, 157: 26–40.
[39] OLIVER C, QUEGAN S. Understanding synthetic aperture radar images. Raleigh: SciTech Publishing, 2004.
[40] PIERACCINI M, MICCINESI L. Ground-based radar interferometry: a bibliographic review. Remote Sensing, 2019, 11(9): 1029.
[41] TOFANI V, RASPINI F, CATANI F, et al. Persistent scatterer interferometry (PSI) technique for landslide characterization and monitoring. Remote Sensing, 2013, 5(3): 1045–1065.
[42] ZHANG H. Research on DInSAR method based on coherent target. Beijing: Science Press, 2009. (in Chinese)
[43] WANG J F, PENG J H, YANG H L, et al. InSAR phase unwrapping algorithm based on improved integral method. Science of Surveying and Mapping, 2016, 41(12): 85–88.
[44] LIU G X, CHEN Q, LUO X J, et al. Radar interference theory and method based on permanent scatterer. Beijing: Science Press, 2012. (in Chinese)
[45] ZEBKER H A, LU Y. Phase unwrapping algorithms for radar interferometry: residue-cut, least-squares, and synthesis algorithms. Journal of the Optical Society of America A, 1998, 15(3): 586–598.
[46] ZHA X J, SHAO Z G, DAI Z Y, et al. Accurate frequency estimation for removal of orbital fringes in SAR interferograms. International Journal of Remote Sensing, 2020, 41(14): 5305–5320.
[47] TIAN X, LIAO M S. The analysis of conditions for InSAR in the fifield of deformation monitoring. Chinese Journal of Geophysics, 2013, 56(3): 812–823. (in Chinese)
[48] GUO L P, YUE J P. Analysis coherence effected by baseline and time interval. Bulletin of Surveying and Mapping, 2018, 7: 9–12.
[49] TOUZI R, LOPES A. Coherence estimation for SAR imagery. IEEE Trans. on Geoscience and Remote Sensing, 1999, 37(1): 135–149.
[50] ZEBKER H A, VILLASENOR J. Decorrelation in interferometric radar echoes. IEEE Trans. on Geoscience and Remote Sensing, 1992, 30(5): 950–959.
[51] BIGGS J, WRIGHT T, LU Z, et al. Multi-interferogram method for measuring interseismic deformation: Denali fault, Alaska. Geophysical Journal of the Royal Astronomical Society, 2010, 170(3): 1165–1179.
[52] LI Q Y, WANG N C. Numerical analysis. Beijing: Tsinghua University Press, 2008.
[53] XU Q, DONG X J, LI W L. Integrated space-air-ground early detection, monitoring and warning system for potential catastrophic geohazards. Geomatics and Information Science of Wuhan University, 2019, 44(7): 957–966. (in Chinese)
[54] HUANG Z S, SUN J P, LI Q, et al. Time and space varying atmospheric phase correction in discontinuous ground-based synthetic aperture radar deformation monitoring. Sensors, 2018, 18(11): 3883.

Biographies

LEI Tianjie was born in 1984. He received his Ph.D. degree from Beijing Normal University in 2015. He is mainly engaged in the research of reservoir dam and ecology security in the basin based-on air-space-ground big data.
E-mail: leitj@iwhr.com

WANG Jiabao was born in 1990. She received her M.S. degree in architecture and civil engineering from North China University of Water Resources and Electric Power in 2017. She is currently pursuing her Ph.D. degree at China University of Mining & Technology, Beijing. Her research interests include remote sensing monitoring, flood and drought disaster monitoring and assessment.
E-mail: Jiabao_wang@126.com

HUANG Pingping was born in 1978. He received his Ph.D. degree in engineering from Institute of Electronics, Chinese Academy of Sciences in 2010. He is currently the deputy dean of the School of Information Engineering, Inner Mongolia University of Technology. His research interests include radar system, radar signal processing, and microwave remote sensing.
E-mail: hpp@imut.edu.cn

TAN Weixian was born in 1981. He received his Ph.D. degree from University of Chinese Academy of Sciences, Beijing, China, in 2009. From 2009 to 2014, he was an associate researcher with the Science and Technology on Micro-wave Imaging Laboratory, Institute of Electronics, Chinese Academy of Sciences. Since 2015, he has been a professor with the College of Information Engineering, Inner Mongolia University of Technology. His main research interests are airborne synthetic aperture radar (SAR)/ 3D SAR system and signal processing.
E-mail: wxtan@imut.edu.cn

QI Yaolong was born in 1984. He received his Ph.D. degree in the Institute of Electrics, Chinese Academy of Sciences, Beijing in 2012. He is a professor with the College of Information Engineering, Inner Mongolia University of Technology. His current research interests include radar signal and information processing, radar system application and ground-based radar system.
E-mail: qiyaolong@imut.edu.cn

XU Wei was born in 1983. He received his M.S. degree from Nanjing Research Institute of Electronics Technology, Nanjing, China, in 2008 and Ph.D. degree in communication and information engineering from Graduate University of Chinese Academy of Sciences, Beijing, China, in 2011. In 2011, he joined the Department of Spaceborne Microwave Remote Sensing System, Institute of Electronics, Chinese Academy of Sciences, Beijing. Since 2018, he has been currently a professor with the College of Information Engineering, Inner Mongolia University of Technology. His research interests include spaceborne/SAR technology for advanced modes, SAR raw signal simulation, and SAR signal processing.
E-mail: xuwei1983@imut.edu.cn

ZHAO Chun was born in 1975. He received his Ph.D. degree from China Institute of Water Resources and Hydropower Research in 2010. He is mainly engaged in the research of dam safety monitoring data analysis and dam safety evaluation.
E-mail: zhaochun@iwhr.com